



Tensile properties and damage evolution in vascular 3D woven glass/epoxy composites



Anthony M. Coppola^{a,b}, Piyush R. Thakre^{b,c}, Nancy R. Sottos^{b,d}, Scott R. White^{a,b,*}

^a Department of Aerospace Engineering, University of Illinois at Urbana-Champaign, Urbana, IL 61801, USA

^b Beckman Institute for Advanced Science and Technology, University of Illinois at Urbana-Champaign, Urbana, IL 61801, USA

^c Dow Chemical Company, Midland, MI 48642, USA

^d Department of Material Science and Engineering, University of Illinois at Urbana-Champaign, Urbana, IL 61801, USA

ARTICLE INFO

Article history:

Received 11 October 2013

Received in revised form 10 December 2013

Accepted 14 December 2013

Available online 21 December 2013

Keywords:

A: 3-Dimensional reinforcement

B: Mechanical properties

D: Optical microscopy

Microvascular

ABSTRACT

Vascularization enables multifunctional composites capable of self-healing, thermal regulation, electrical and magnetic modulation, and damage sensing. In this study, the effect of vascular channels on the in-plane tensile properties and damage progression of three-dimensional orthogonally woven textile composites is examined. Vascular channels are manufactured by Vaporization of Sacrificial Components (VaSC). Sacrificial fibers composed of poly(lactic acid) treated with tin(II) oxalate catalyst are integrated into 3D woven glass fiber preforms. Composites with straight channel and undulating wave-shaped channel architectures are created and tested in both longitudinal and transverse orientations. Damage evolution is monitored by acoustic emission and optical microscopy. Vascular channels have minimal effect on tensile behavior when fiber alignment is unaltered, while reductions in strength and modulus and increased crack density occur when channels distort the reinforcement fiber architecture.

© 2013 Elsevier Ltd. All rights reserved.

1. Introduction

In nature, complex organisms rely on circulatory networks to carry out critical functions such as wound healing, nutrient delivery, cellular waste removal, and thermal regulation. Inspired by these examples, structural polymers and fiber-reinforced composites incorporating networks of internal vascular channels have been developed [1–10]. Vascular networks in composites deliver fluids to achieve a range of functions including self-repair [2–5], thermal management [6,7], electrical and magnetic modulation [1], and damage detection [8–10].

In bulk polymers, vascular networks have been fabricated by electrostatic discharge [11], direct-ink writing of fugitive inks [3,12], wire removal through melting or manual extraction [2,13–15], hollow glass fiber (HGF) integration [9,10,16–19], and Vaporization of Sacrificial Components (VaSC) [1,20]. Of these methods, only wire removal, HGF, and VaSC methods are viable for fiber-reinforced polymer composite materials. Wire removal and HGFs are restricted to straight channels with one-dimensional connectivity. In contrast, the VaSC method can be integrated directly into the textile preforming process to create 3D, interconnected architectures [1].

The introduction of vascular channels influences the mechanical properties of laminated composites, including fracture toughness

[13,17,21], compressive and tensile properties [16,22], flexural properties [18], and impact damage resistance [2,10,14,19,23]. Kousourakis et al. examined the effect of shape, size, and orientation of HGFs on the in-plane tensile and compressive modulus and ultimate strength of a non-woven carbon/epoxy laminate system [16]. Channels oriented transverse to the loading axis caused a larger drop in tensile and compressive properties compared to longitudinally oriented channels. This reduction was attributed to local misalignment of the load-bearing fibers caused by the presence of the channels in the laminate. Larger HGF diameters corresponded to increased fiber misalignment and a greater decrease in properties. Huang et al. conducted a similar study, focusing only on the compressive properties of non-woven carbon/epoxy laminates containing channels manufactured using a steel wire removal technique [22]. Experimental and finite-element analyses supported the results reported by Kousourakis et al. [16].

Woven textile composites are used extensively in industrial applications, including ballistic armor, marine vessels, wind energy, automotive, and aerospace [24]. Yet, no studies at this time have examined the effect of vascular networks on the mechanical properties of woven textile composites. While 2D textiles contain fibers that are predominately oriented in a single plane, in 3D textiles some fibers are oriented in the out-of-plane direction. Lomov et al. [25] compared the tensile properties of 2D plain weave and 3D orthogonally woven textiles and concluded that 3D textiles have superior in-plane strength and modulus. In a related study, Ivanov et al. [26] reported that 3D textiles are able

* Corresponding author. Address: 306 Talbot Laboratory, 104 South Wright Street, Urbana, IL 61801, USA. Tel.: +1 217 333 1077.

E-mail address: swhite@illinois.edu (S.R. White).

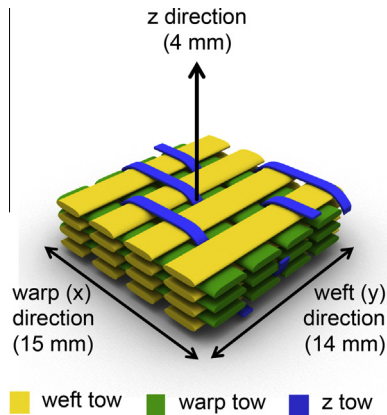


Fig. 1. A schematic of the three-dimensional orthogonally woven S-2 glass fiber textile. The textile is composed of 3 warp layers and 4 weft layers, which are held together by the z-fibers. The areal density of the fabric is 4.07 kg/m^2 (120 oz/yd^2). In the warp layers there are 3.0 tows/cm , whereas in the weft layers there are 2.7 tows/cm . As a result of the difference in tow density, the fiber content in the x and y directions are nearly equivalent. (For interpretation of the references to color in this figure legend, the reader is referred to the web version of this article.)

to absorb more energy while suppressing delaminations and tow-matrix interfacial cracking.

Here, we examine the mechanical properties and damage progression in a vascularized 3D woven textile composite subject to in-plane tension. Channels are manufactured using VaSC with a diameter of $500 \mu\text{m}$, which is chosen to roughly match the diameter of a fiber tow. Two different vascular architectures are examined including straight channels and undulating wave shaped channels, each featuring similar channel volume fractions (V_c). Tests are conducted with channels oriented in both the longitudinal and transverse direction relative to the loading axis.

2. Specimen manufacturing

2.1. Sacrificial fiber synthesis

Sacrificial fibers (SF) for the VaSC process were prepared from $500 \mu\text{m}$ diameter poly(lactic acid) (PLA) monofilament fibers

(Teijin Monofilament, Inc.) following the procedure established by Esser-Kahn et al. [1] and Dong et al. [20]. In this procedure, the commercial PLA fibers were treated with tin(II) oxalate (SnOx) catalyst to decrease their thermal degradation temperature from approximately 280°C to 200°C [1]. The as received fibers were wound on a custom reel and placed in a catalyst treatment bath composed of 480 mL trifluoroethanol (TFE, Sigma–Aldrich), 320 mL deionized water, 13 g SnOx (Sigma–Aldrich), 40 mL Disperbyk 187 (BYK Chemie), and 1 g Rhodamine 6G dye (Sigma–Aldrich). The beaker containing the catalyst solution was suspended in a temperature-controlled water bath and the reel was attached to a digital mixer, which agitated the solution at $400\text{--}450 \text{ RPM}$ for 24 h at 37°C . Following the treatment process, the fibers were dried in a convection oven for 24 h at 35°C .

2.2. Composite specimen manufacture

Composite specimens were manufactured using a single layer of 3D orthogonally woven S2-glass fibers with an areal density of 4.07 kg/m^2 (120 oz/yd^2) (TEAM Inc.), shown schematically in Fig. 1. The SFs were manually incorporated into the glass fiber textile by hand using a sewing needle to guide the SF through the fabric. No glass fibers were removed to accommodate the SFs. Three types of specimens were created for testing: (1) control specimens with no channels, (2) specimens with channels that follow a straight trajectory, and (3) specimens with channels that follow a wave shaped trajectory. The location of the SFs in the unit cell of the glass fiber textile for each of specimen is shown schematically in Fig. 2. For specimens with straight channels, the SF was placed adjacent to the z-fiber along the path of a warp tow. For specimens with wave channels, the SF followed the path of the z-fiber but was translated half the distance of the unit cell in the warp direction. In both cases the SF traversed the interstitial region between the warp tows. As such, there is no change in fiber volume fraction (V_f) locally around a channel although for the wave architecture some displacement of glass fibers is apparent (Fig. 2).

The S2-glass/SF preform was infused with epoxy resin using a vacuum assisted resin transfer molding (VARTM) process. The resin was composed of EPON 862 epoxy mixed with EPIKURE W curing agent (Miller-Stephenson) in a weight ratio of 100:26.4,

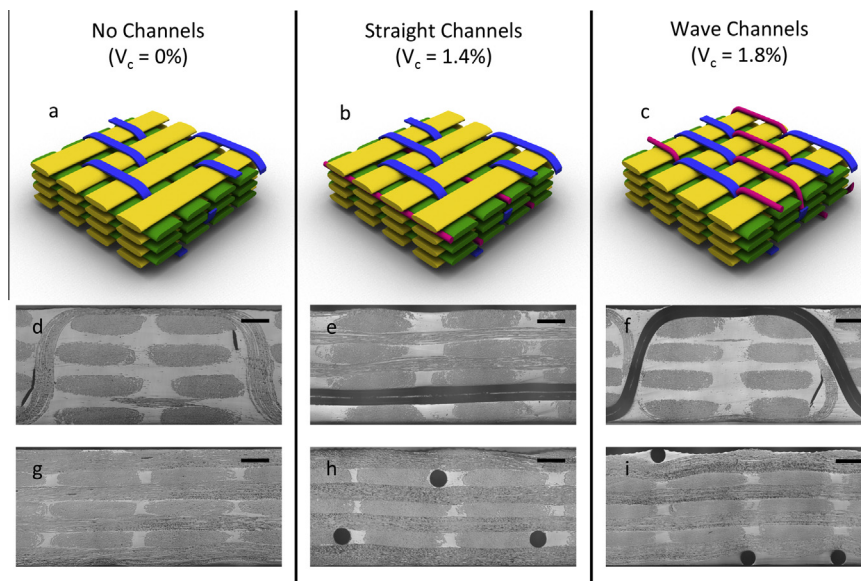


Fig. 2. The three different types of specimens examined. Schematics of the unit cell of the preforms (a–c) show the weft tows in yellow, the warp tows in green, the z-fibers in blue, and the sacrificial fibers in red. Optical micrographs ($2.5\times$ lens) (d–f) show surfaces normal to the warp direction and (g–i) surfaces normal to the weft direction. Scale bars represent 1 mm . (For interpretation of the references to color in this figure legend, the reader is referred to the web version of this article.)

respectively. Prior to the infusion, the resin was degassed for 2 h at 80 °C and the preform was preheated to 100 °C, to reduce the viscosity of the resin during the infusion. The part was insulated on the top surface and then cured on a hot plate at 121 °C for 2 h followed by 177 °C for 2 h. Due to the long gel time and low viscosity of the resin at elevated temperatures, a double bag method was employed to prevent excess resin from being removed from the part during the curing cycle. Control panels without vascular channels had an average V_f of $44.5 \pm 1.3\%$. After the initial cure of the resin, SFs were vaporized in the appropriate specimens by cutting the panel to expose the ends of the SFs, then heating the panel in a vacuum oven at 200 °C for 48 h. Following the heat treatment and SF removal, a slight browning of the matrix material occurred and was attributed to oxidation of the resin.

Following the cure cycle, stress cracks were observed near bends of the z-fiber in all specimens, as seen in Fig. 2(d and f). The stress cracks are a result of the normal curing cycle and were not observed to grow during subsequent heat treatment of the composite. Stress cracking was consistent in both vascularized and non-vascularized specimens.

Two types of control (no channel) specimens were used to isolate the effect of the heat treatment on the composite properties. One set of control specimens was cured using the normal curing cycle, while a second set was also subjected to a post-cure at 200 °C for 48 h under vacuum. For vascular specimens, both the straight and wave channel specimens were post-cured at 200 °C for 48 h under vacuum to remove the SF. Tensile specimens were cut from the composite panels with the channels oriented longitudinal and transverse to the axis of loading (Fig. 3), corresponding to the warp and weft directions of the fabric, respectively. In both cases, the channel trajectory followed the warp direction of the fiber preform. Fiber orientation in control specimens matched that of the vascular specimens for longitudinal and transverse tensile testing.

2.3. Epoxy specimen manufacture

Testing was performed to investigate the effects of the post-cure used to vaporize the SFs on the mechanical properties of the epoxy matrix phase of the composite. Specimens were manufactured from EPON 862 epoxy/EPIKURE W curing agent (Miller-Stephenson) mixed in a weight ratio of 100:26.4, degassed for 2 h at 80 °C, then cured in a convection oven at 121 °C for 2 h followed by 177 °C for 2 h in closed molds. The closed mold design helped to minimize oxidation of the resin during curing, but browning similar to the composite specimens was still observed. One group of specimens was subjected only to the epoxy cure cycle, and the other group was subjected to an additional 200 °C for 48 h post-cure under vacuum.

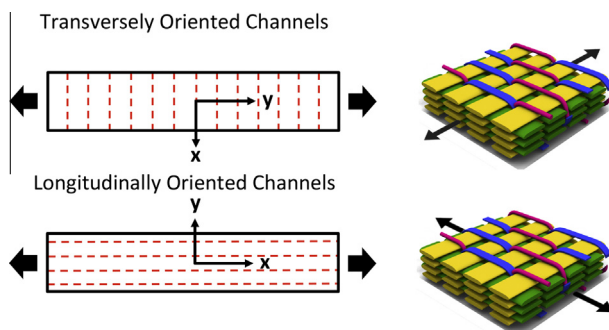


Fig. 3. Transverse and longitudinal testing orientations, shown schematically (left) and relative to the textile unit cell (right). In the schematic, the channel direction is represented by red dashed lines. (For interpretation of the references to color in this figure legend, the reader is referred to the web version of this article.)

3. Experimental procedure

3.1. Composite tension and acoustic emission testing

Composites specimens were prepared and tested in tension according to ASTM D3039. A schematic showing the relevant dimensions and setup of the specimen is shown in Fig. 4. To minimize stress concentrations from the grips, aluminum end tabs were attached to the specimen using an epoxy adhesive (Hysol EA 9309.3NA, Henkel Corp.) cured at 82 °C for 1 h. All tests were performed on a universal electromechanical test frame (Instron 4483) under displacement control at a rate of 1 mm/min. A sample plot of stress and acoustic emissions (AE) versus strain is shown in Fig. 5. Strain was measured using a 25.4 mm gage length extensometer, held in place on the specimen using built-in clips. Ultimate tensile stress (σ_u) was calculated based on the maximum load attained by the specimen, which was generally followed by an abrupt drop in load indicating failure. Young's modulus (E) was measured in the linear portion of stress–strain curve, between 0.1% and 0.3% strain.

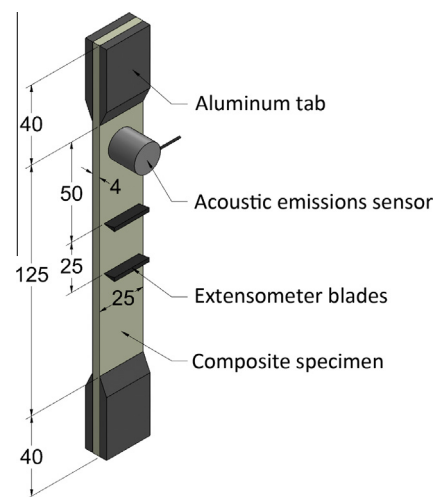


Fig. 4. Schematic of the tensile test specimen showing relevant dimensions and the placement of the extensometer and acoustic emissions sensor. Dimensions are in millimeters. (For interpretation of the references to color in this figure legend, the reader is referred to the web version of this article.)

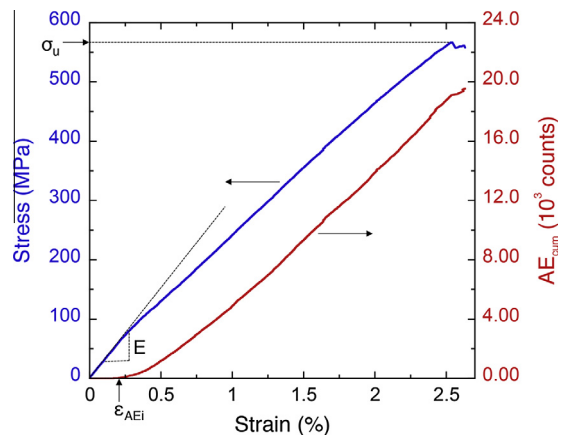


Fig. 5. A sample plot of stress and cumulative acoustic emissions (AE_{cum}) versus strain. Locations used to record ultimate tensile stress (σ_u), Young's modulus (E), and strain at damage initiation (ϵ_{AEI}) are marked on the plot. (For interpretation of the references to color in this figure legend, the reader is referred to the web version of this article.)

Table 1
Results of composite specimen tensile testing^a.

		Tests ^b (#)	<i>t</i> (mm)	<i>E</i> (GPa)	<i>E</i> _{norm} ^c (GPa)	σ_u (MPa)	σ_{norm} ^c (MPa)	ϵ_{AEi} (%)
<i>Longitudinal (Warp) loading orientation</i>								
Control specimens	Normal cure	9	3.79 ± 0.11	21.5 ± 1.7	21.7 ± 1.5	567 ± 10	563 ± 14	0.28 ± 0.07
	Post-cured	5	3.76 ± 0.12	21.6 ± 1.4	21.5 ± 0.7	547 ± 41	546 ± 29	0.27 ± 0.05
Vascular specimens	Straight channel	9	3.80 ± 0.09	22.5 ± 1.6	22.7 ± 1.4	546 ± 16	544 ± 14	0.23 ± 0.04
	Wave channel	9	3.98 ± 0.05	20.4 ± 1.8	21.6 ± 1.9	489 ± 20	516 ± 23	0.22 ± 0.03
	<i>P</i> -value	–	–	–	0.338	–	0.021	0.101
<i>Transverse (Weft) loading orientation</i>								
Control specimens	Normal cure	9	3.76 ± 0.09	25.9 ± 1.6	25.9 ± 1.4	566 ± 24	566 ± 39	0.26 ± 0.03
	Post-cured	5	3.74 ± 0.10	24.6 ± 2.4	24.5 ± 2.6	548 ± 28	544 ± 14	0.25 ± 0.03
Vascular specimens	Straight channel	9	3.89 ± 0.06	24.0 ± 1.5	24.8 ± 1.3	558 ± 28	580 ± 36	0.21 ± 0.03
	Wave channel	9	3.98 ± 0.04	21.9 ± 1.8	23.2 ± 2.1	470 ± 35	497 ± 39	0.21 ± 0.06
	<i>P</i> -value	–	–	–	0.032	–	0.007	0.037

^a Error bounds correspond to one standard deviation. *P*-values from ANOVA are included, which indicate a significant difference among the specimen categories when $P \leq 0.05$.

^b Only five tests were used to evaluate strength for each specimen category.

^c Values are normalized by thickness, i.e. multiplied by t/t_{avg} .

The AE sensor (Dunegan Engineering Company, Inc. Model SE2MEG-P) was adhered to the test specimen using vacuum grease in the gage section (see Fig. 4). A DC power supply (Model GW INSTEX GPC-3030D 8 V) provided excitation and AE signals were amplified using a DECI preamplifier (Model 400p-20H, +28 V DC). A National Instruments digital acquisition system (NI-DAQ-USB-6251) recorded the AE signals with a sampling rate of 500 kHz. Voltage and time data was recorded for all events and correlated with strain data from mechanical testing using corresponding time stamps from AE and tension test data. In all of the specimens, acoustic events initiated after some threshold strain was reached, denoted by ϵ_{AEi} .

For the controls, straight channel, and wave channel specimens, a total of nine specimens were tested in each loading orientation. Five of the specimens were tested to failure and four specimens were loaded to intermediate stress levels (100 MPa, 250 MPa, 350 MPa, 450 MPa) and then unloaded. After unloading, these specimens were imaged using transmission optical photography. For the post-cured controls (no channels) all tests were conducted to failure.

3.2. Epoxy tension and DMA testing

Epoxy tensile tests were conducted according to ASTM D638 using type I polymer tensile bars. Tests were performed on a universal electromechanical test frame (Instron 4483) under displacement control at a rate of 1 mm/min. Strength was based on the maximum load achieved prior to ultimate failure (σ_u). Young's modulus (*E*) was measured between 0.1% and 0.3% strain for all specimens. Dynamic mechanical analysis (DMA) was carried out according to ASTM D7028 using a three-point bend test procedure to measure the glass transition temperature (T_g). Specimens were cut to 35 mm long, 6 mm wide and 2 mm thick (25 mm span distance) and oscillated at 0.1% maximum strain at 1 Hz during a temperature ramp from 25 to 250 °C at 5 °C/min. Five tests were performed for each specimen category for tensile testing and two specimens were tested for each specimen category for DMA testing.

3.3. Statistical analysis of data

Young's modulus, strength, and strain at damage initiation in each loading orientation were examined using analysis of variance (ANOVA) to determine if significant differences existed among specimen categories [27]. The *F* statistic is first calculated as

$$F = \frac{MS_B}{MS_W} \quad (1)$$

where MS_B is the between-group variability and MS_W is the within-group variability. These values are defined as,

$$MS_B = \frac{\sum_i n_i (\bar{Y}_i - \bar{Y})^2}{K - 1} \quad (2)$$

$$MS_W = \frac{\sum_{ij} (Y_{ij} - \bar{Y}_i)^2}{N - K} \quad (3)$$

where \bar{Y}_i is the sample mean of the *i*-th group, \bar{Y} is the overall mean, Y_{ij} is the *j*-th observation in the *i*-th group, n_i is the number of observations in the *i*-th group, *k* is the number of groups, and *N* is the total sample size. Based on *F*, the *P*-value is calculated using the Fisher-Snedecor distribution (*F*-distribution). The condition indicating a statistically significant difference exists among the test groups is

$$P \leq P_{critical}, \quad (4)$$

where $P_{critical}$ is equal to the chosen significance level. Unless otherwise noted, a 5% significance level ($P_{critical} = 0.05$) was used.

ANOVA only tests for significant differences globally. Outlying specimen categories were identified using a Tukey range test based on the Tukey–Kramer procedure, which instead considers pairwise comparisons. The test statistic for the Tukey range test is

$$q = \frac{|Y_A - Y_B|}{\sqrt{\frac{MS_W}{2} \left(\frac{1}{n_a} + \frac{1}{n_b} \right)}}, \quad (5)$$

where Y_A and Y_B are the means of the two groups under consideration and n_a and n_b are the sample size of each group. The *P*-value can be calculated from the value of *q* using the studentized range distribution and is again evaluated using Eq. (4) for statistical significance. More detailed information on ANOVA and the Tukey range test can be found in Salkind [27].

4. Results and discussion

4.1. Tension test

The average tensile strength, Young's modulus, and strain at damage initiation for the composite specimens are summarized in Table 1 and Fig. 6. *P*-values from the ANOVA test are included in Table 1, with values below 0.05 indicating a statistically significant difference exists between the four categories. In addition, *P*-values from the Tukey range test (P_{Tukey}) are noted throughout the discussion where relevant. The error bounds on modulus and strength were 4.8% and 7.6% of the mean values, respectively.

The primary sources of error were small variations in fiber alignment and tow spacing in the textile fabric. Callus et al. [28] reported that orthogonally woven glass fiber textiles have fiber misalignments up to 5.1° and 5.7° (within the 90th percentile) in the warp and weft directions, respectively. Distortions of the tow spacing occur due to handling of the textile during transportation, cutting, and infusion. These distortions to the textile were minimized where possible, but some variation was still observed.

Wave channel were thicker than all other specimen types because of through thickness stiffening of the fabric and therefore had higher resin content. Alternatively, straight channel specimens were the same thickness as controls because the SFs fit into the interstitial region between the warp and weft tows. In order to compare results across all specimen types the tensile properties were normalized with respect to thickness by multiplying the raw data by t/t_{avg} , where t_{avg} is the average thickness of the control specimens. This process is analogous to normalizing by fiber volume fraction. Both non-normalized and normalized data are included in Table 1.

Comparison of the normally cured and post-cured control specimens indicated no statistically significant reductions in strength or modulus as a consequence of the 48 h 200 °C post-cure. Polymer tensile testing also confirmed that post-curing did not degrade the tensile properties (Table 2) although an increase in glass transition temperature from 130 °C to 140 °C was observed. Tensile properties were not affected by the presence of straight channels. No statistically significant reductions were observed for wave channel specimens when compared to post-cured controls. However, the wave channel architecture did impart statistically significant reductions based on Eq. (4) in longitudinal strength ($P_{Tukey} = 0.013$), transverse modulus ($P_{Tukey} = 0.019$), and transverse strength ($P_{Tukey} = 0.025$) compared to normally cured control specimens, although longitudinal modulus remained unchanged. Hence, the only significant reduction in tensile properties occurred for the wave channel architecture when compared to normally cured control samples.

The AE data shows earlier initiation of damage for vascular specimens compared with the controls. The mean strain at damage initiation was approximately 20% lower for those specimens containing channels. Using the ANOVA test, no significant change was found in the longitudinal direction for any of the specimens, whereas in the transverse direction the change was significant to a 5% significance level, but insignificant to a 1% significance level. These results suggest that the changes in strain at damage initiation were likely insignificant. Furthermore, there is no correlation between the early onset of AE in the vascularized composites and lower strength. In the straight channel specimens, the average strain at damage initiation was the same as for the wave channel specimens in both orientations, signaling that damage initiates at the same strain for both channel architectures. Interestingly, the strength of the straight channel specimens was equal to that of the controls, while a drop was observed for the wave channel specimens. The early onset of AE does not directly correlate to reduced strength, indicating other mechanisms may be responsible for the reduction in strength in the wave channel specimens.

4.2. Evolution of damage

Transmitting light photographs showing damage progression in control, straight channel and wave channel specimens are shown in Figs. 7 and 8 for the transverse and longitudinal loading orientations, respectively. The dominant damage mechanism observed for all specimens was transverse cracking, indicated by straight, vertical dark lines in the images. As expected, transverse cracking

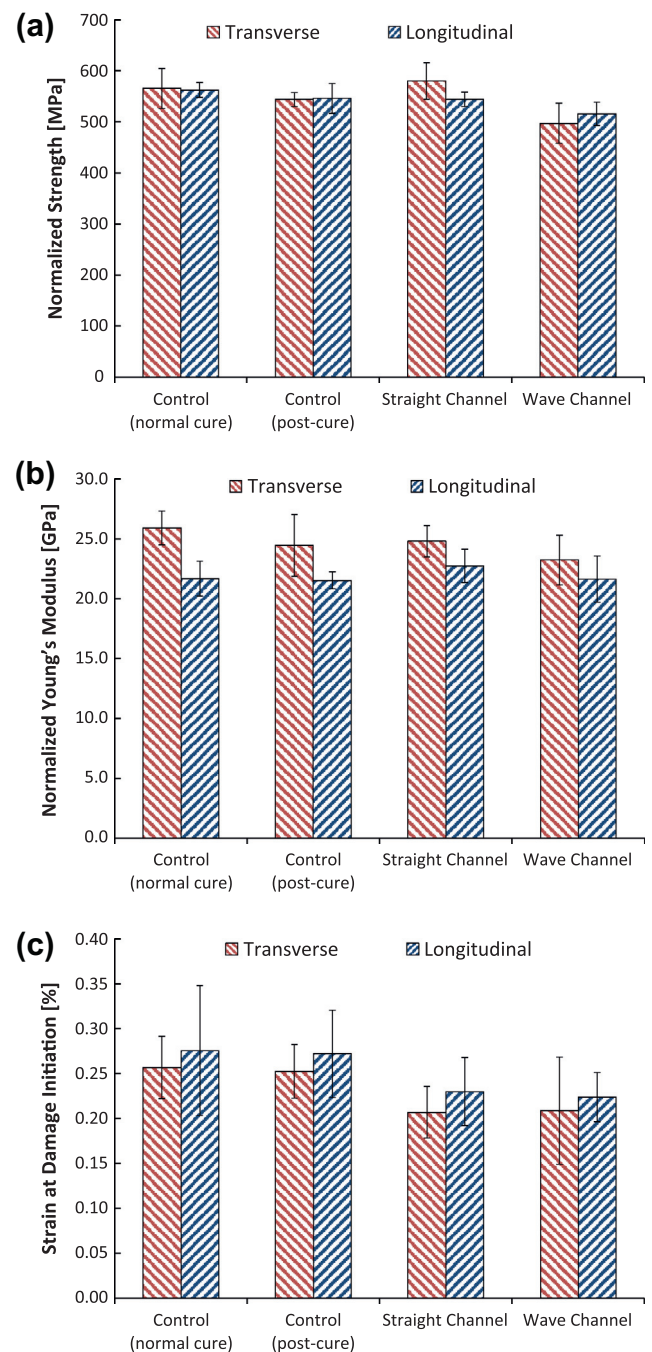


Fig. 6. Results of tensile testing: (a) normalized strength, (b) normalized Young's modulus, and (c) strain at damage initiation. (For interpretation of the references to color in this figure legend, the reader is referred to the web version of this article.)

Table 2

Results of tensile and DMA tests performed on neat epoxy specimens^a.

Post-cure condition	E (GPa)	σ_u (MPa)	T_g (°C)
No post-cure	2.86 ± 0.05	68.6 ± 8.3	130
48 h @ 200 °C	2.81 ± 0.12	70.2 ± 3.7	140

^a Error bounds correspond to one standard deviation for tensile testing. No error bounds are shown for glass transition temperature because only two tests were performed, which yielded values differing by less than 1 °C.

density steadily increases with loading. Fig. 9 contains a representative cross section revealing the transverse cracks in a longitudinally loaded wave channel specimen.

4.2.1. Transversely oriented channels

In the transversely loaded specimens, a repeating pattern of dark regions (spots) develops as stress increases (Fig. 7). The location of these dark spots corresponds to the location of the z-fiber on the bottom surface of the specimen, near the light source. These spots initiate at lower stress levels in the wave channel specimens compared to either the control or the straight channel specimens. By 250 MPa, the dark spots are fully visible in the wave channel specimens, whereas in the other categories they only begin to appear in some locations at 350 MPa and then are fully apparent at 450 MPa. Polished cross sections taken from the location of these dark spots for all three categories are shown in Fig. 10. The dark regions observed in transmission imaging correspond directly

to areas of cracking under weft tows adjacent to the z-fibers (labeled A) and channels (labeled B). In all three categories, interfacial cracking between the weft tows and the matrix occurs in the layer adjacent to the z-fiber (A). In the wave channel specimens, there are similar but much larger cracks in the weft tows adjacent to the channel (B), in addition to those near the z-fiber.

The cracking in Fig. 10 is attributed to misalignment of the weft tows caused by the z-fibers and channels. As shown in Fig. 11, the presence of the z-fiber causes a small misalignment in the z-direction of the adjacent weft tow (approximately 3–6°), while the wave channels lead to a much larger misalignment (approximately 11–17°). In addition to the misalignment in the thickness direction there is an in-plane misalignment of the weft tows,

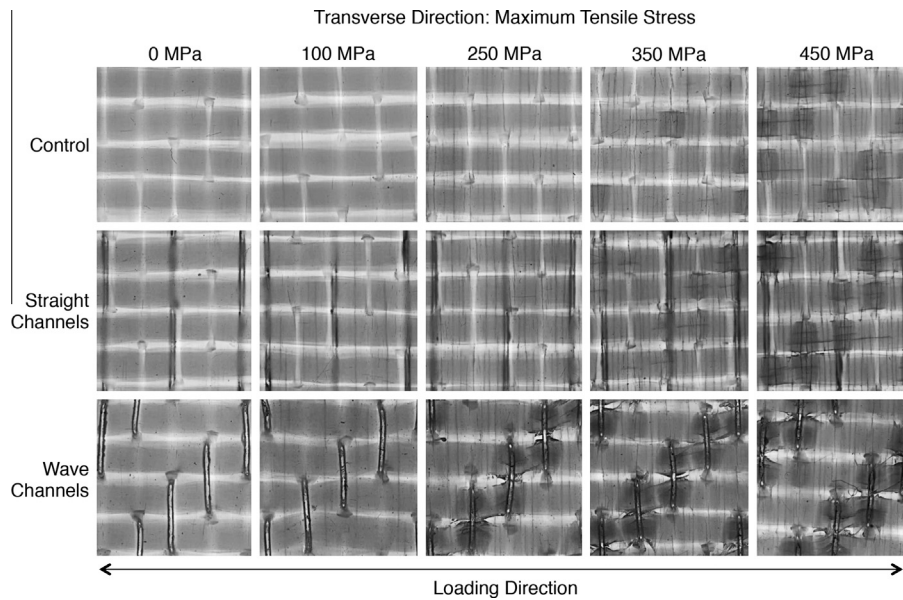


Fig. 7. Damage development in transverse specimens loaded to intermediate stress levels imaged by transmitting light photography. Two damage modes were observed: transverse cracking, which shows up as thin vertical dark lines in the images, and a repeating pattern of dark regions near the z-fibers tows and channels indicative of weft tow cracks near these features. Each image represents a 15 mm × 15 mm area.

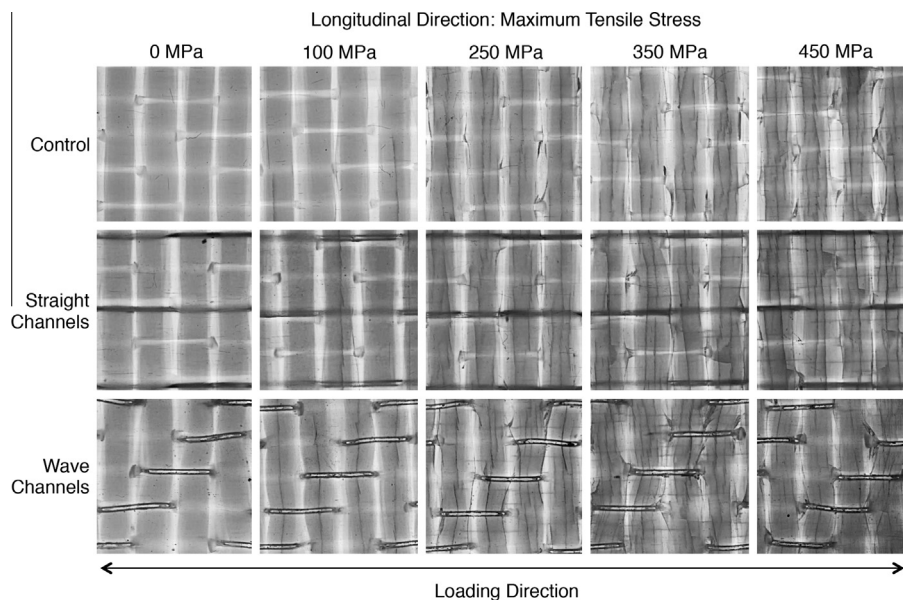


Fig. 8. Damage development in longitudinal specimens loaded to intermediate stress levels imaged by transmitting light photography. Transverse cracking was the only damage mode observed, which shows up as thin vertical dark lines in the images. Each image represents a 15 mm × 15 mm area on the sample.

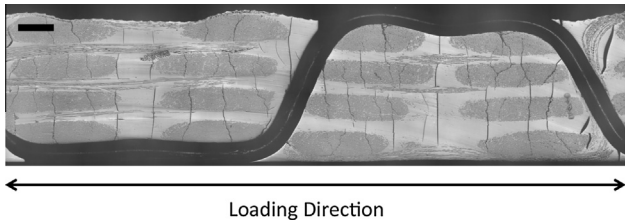


Fig. 9. Optical micrograph (2.5× lens) of transverse cracking in a longitudinally oriented wave channel specimen loaded to 450 MPa. Scale bar represents 1 mm.

caused by excessive tension in the SF during processing of the composite (approximately 6–14°) (Fig. 12). Through geometric analysis of these projections in the *x*-*z* and *y*-*z* planes, we can estimate the total misalignment of a weft tow relative to the *x*-axis as approximately 12–21° due to the presence of the wave channels. In contrast, the straight channels do not cause measurable misalignment of the weft tows because they fit in the interstitial spacing between the warp tows.

The misalignment of the fibers around a wave channel leads to cracking in the adjacent weft tow as a result of through thickness stresses that are developed. The fiber curvature in the misaligned region causes tensile stress perpendicular to the loading axis due to the tendency of the fiber to realign in the direction of loading. More extensive cracking is observed around the wave channels than around the *z*-fibers. Similar observations are made by Huang et al. [22] and Kousourakis et al. [16] in laminate composite systems with vascular channels loaded in compression and tension, respectively. In both of these studies, increased fiber misalignment caused by the presence of the channels correlates with larger reductions in properties and increased cracking in regions directly surrounding the channel.

The fiber misalignment induced by the transversely oriented wave channels reduces the tensile properties through two interacting mechanisms. First, cracks formed as a result of fiber misalignment reduce the load carrying capacity of the composite locally and generate stress concentrations around the cracks. Second,

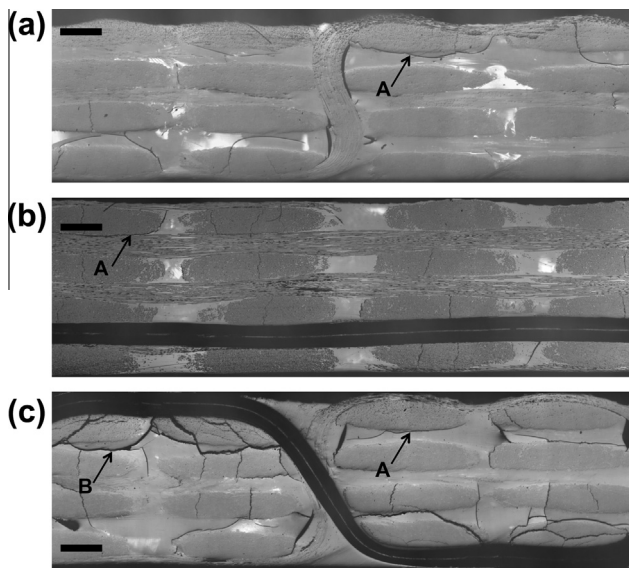


Fig. 10. Optical micrographs (2.5× lens) of transversely oriented (a) control, (b) straight channel, and (c) wave channel specimens loaded to 450 MPa. Cracking was observed under the *z*-fibers in all specimens (A), while larger cracks were additionally observed under the wave channels (B). The loading axis is directed out of the page. Scale bar represents 1 mm.

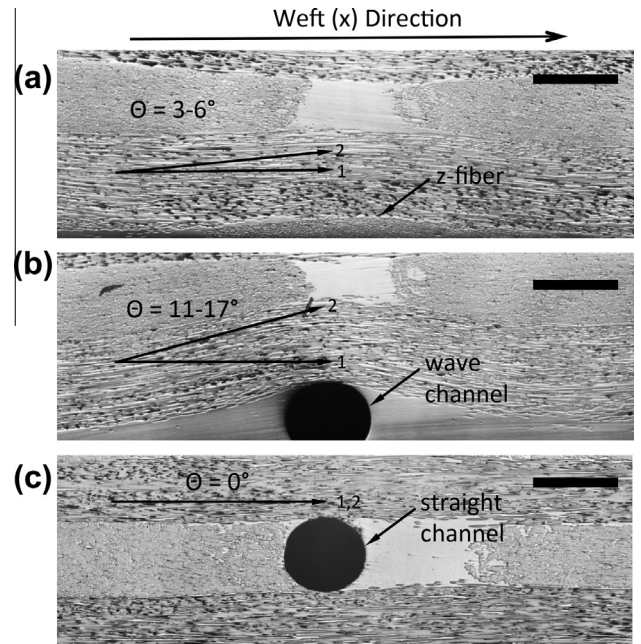


Fig. 11. Optical micrographs (2.5× lens) comparing weft tow misalignment due to the (a) *z*-fiber, (b) wave channel, and (c) straight channel. Scale bar represents 0.5 mm.

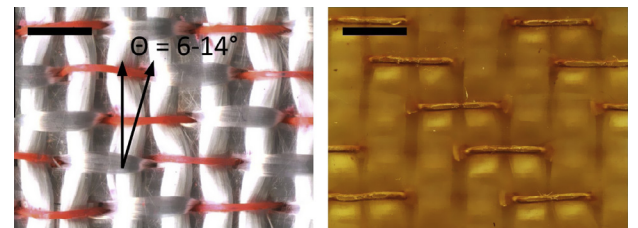


Fig. 12. (Left) The fiber textile containing SFs integrated in a wave shape showing the effect of glass fiber crimping due to the SF. (Right) The same preform after being infused with epoxy showing the crimping still remains present. Scale bar represents 5 mm. (For interpretation of the references to color in this figure legend, the reader is referred to the web version of this article.)

increased fiber misalignment relative to the axis of loading has a detrimental effect on the in-plane composite properties [16,29]. Weft fiber misalignment in wave channel specimens has a more significant impact on strength than modulus.

Another possible mechanism to explain the reduction in tensile properties for specimens containing transversely oriented channels is the presence of local strain concentrations around the channel. Hamilton et al. [30] reported that transversely oriented channels in a polymeric matrix cause local strain concentrations in the surrounding material. Optical micrographs of specimens loaded up to 100 MPa did not show transverse cracks forming near the transversely oriented channels, providing no evidence that these stress concentrations lead to cracking near the channel. Fibers surrounding the channel may act as reinforcement and prevent crack initiation around the channels. For this reason it is unlikely that stress concentrations associated with the channels are the cause of the reduction in properties observed for transversely oriented channels. Furthermore, no evidence was found that the removal of matrix material to incorporate the channels affects tensile behavior since straight channels did not reduce properties. Rather, changes in tensile properties are largely the result of displacement of the glass fibers from the native textile architecture.

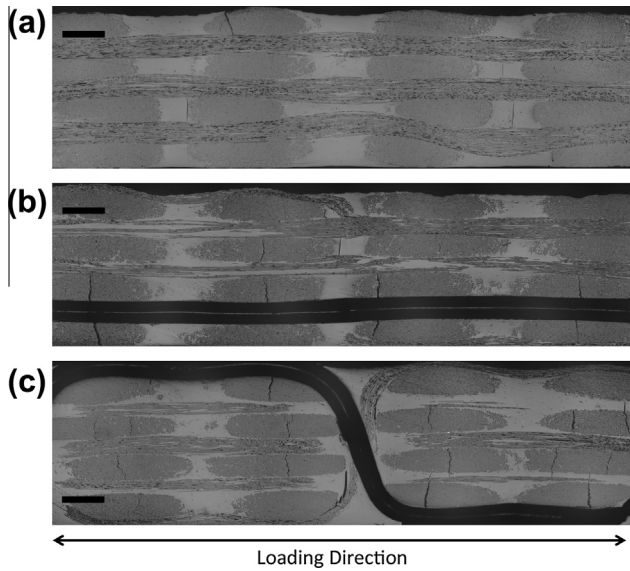


Fig. 13. Optical micrographs ($2.5\times$ lens) of longitudinally oriented (a) control, (b) straight channel, and (c) wave channel specimens loaded to 100 MPa. The wave channel specimen shows increased cracking compared to control and straight channel specimens. Scale bar represents 1 mm.

4.2.2. Longitudinally oriented channels

Damage in specimens loaded longitudinally generally progresses with similar cracking locations and density (Fig. 8), but a notable difference occurs in the 100 MPa images. Transverse cracks are apparent in all of the weft (transversely oriented) fiber tows for wave channel specimens, compared to occasional cracking in the control and straight channel specimens. This observation was further investigated by taking cross-sections of each of these specimens at 100 MPa (Fig. 13). The cross-sections show relatively few cracks in the control and straight channel specimens. In contrast, significant cracking is observed in the wave specimen, with cracks concentrated near the weft tows adjacent to the channel mirroring the same observations found for transversely loaded wave channel specimens. The slight reduction in strength for the longitudinally oriented wave channel specimens is also likely due to stress concentrations caused by the misalignment of the fibers tows.

5. Conclusions

The effect of vascular channels on the in-plane tensile properties and damage progression in a 3D orthogonally woven glass/epoxy composite was examined. Composites with straight and wave shaped channels were produced through vaporization of sacrificial PLA fibers and loaded in both longitudinal and transverse orientations to the channel direction. The post-cure process required for removal of the SF had no effect on the tensile properties of the composite material, despite the required post-cure temperature being significantly higher than the matrix glass transition temperature. Moreover, vascular channels had a negligible effect on the strength, modulus, and damage development when integrated such that no misalignment of the reinforcing fibers occurred (i.e. straight channels), regardless of orientation of loading. When fiber misalignment resulted due to the placement of channels (i.e. wave channels), changes in damage evolution were observed that resulted in modest reductions of strength and modulus that were largely statistically insignificant.

Examination of damage evolution through transmitting light photography and optical microscopy revealed no changes in

damage development when straight channels were integrated into the composite due to minimal distortion of the fiber textile. In contrast, a higher density of cracks initiated under the crest of the wave channels as a consequence of localized fiber misalignment caused by the presence of the wave channel. Acoustic emissions revealed damage initiation at lower average strains for all specimens containing channels, but the large overlapping error in the data diminished the significance of this observation. Overall, the stress concentrations caused by the presence of hollow channels had a minimal effect on damage progression in a 3D woven composite.

Acknowledgements

The authors would like to acknowledge the financial support by Air Force Office of Scientific Research as part of a Multidisciplinary University Research Initiative, Award No. FA9550-09-1-0686, Synthesis, Characterization and Prognostic Modeling of Functionally Graded Hybrid Composites for Extreme Environments.

References

- [1] Esser-Kahn AP, Thakre PR, Dong H, Patrick JF, Vlasko-Vlasov VK, Sottos NR, et al. Three-dimensional microvascular fiber-reinforced composites. *Adv Mater* 2011;23(32):3654–8.
- [2] Norris CJ, Meadway GJ, O'Sullivan MJ, Bond IP, Trask RS. Self-healing fibre reinforced composites via a bioinspired vasculature. *Adv Funct Mater* 2011;21(19):3624–33.
- [3] Toohy KS, Sottos NR, Lewis JA, Moore JS, White SR. Self-healing materials with microvascular networks. *Nat Mater* 2007;6(8):581–5.
- [4] Williams HR, Trask RS, Bond IP. Self-healing sandwich panels: restoration of compressive strength after impact. *Compos Sci Technol* 2008;68(15–16):3171–7.
- [5] Hamilton AR, Sottos NR, White SR. Self-healing of internal damage in synthetic vascular materials. *Adv Mater* 2010;22(45):5159–63.
- [6] Kozola BD, Shipton LA, Natrajan VK, Christensen KT, White SR. Characterization of active cooling and flow distribution in microvascular polymers. *J Intel Mat Syst Str* 2010;21(12):1147–56.
- [7] Soghrati S, Thakre PR, White SR, Sottos NR, Geubelle PH. Computational modeling and design of actively-cooled microvascular materials. *Int J Heat Mass Tran* 2012;55(19–20):5309–21.
- [8] Wu AS, Coppola AM, Sinnott MJ, Chou T-W, Thostenson ET, Byun J-H, et al. Sensing of damage and healing in three-dimensional braided composites with vascular channels. *Compos Sci Technol* 2012;72(13):1618–26.
- [9] Pang JWC, Bond IP. “Bleeding composites”—damage detection and self-repair using a biomimetic approach. *Compos Part A-Appl S* 2005;36(2):183–8.
- [10] Pang JWC, Bond IP. A hollow fibre reinforced polymer composite encompassing self-healing and enhanced damage visibility. *Compos Sci Technol* 2005;65(11–12):1791–9.
- [11] Huang J-H, Kim J, Agrawal N, Sudarsan AP, Maxim JE, Jayaraman A, et al. Rapid fabrication of bio-inspired 3D microfluidic vascular networks. *Adv Mater* 2009;21(35):3567–71.
- [12] Theriault D, White SR, Lewis JA. Chaotic mixing in three-dimensional microvascular networks fabricated by direct-write assembly. *Nat Mater* 2003;2(4):265–71.
- [13] Norris CJ, Bond IP, Trask RS. Interactions between propagating cracks and bioinspired self-healing vasculature embedded in glass fibre reinforced composites. *Compos Sci Technol* 2011;71(6):847–53.
- [14] McCombe GP, Rouse J, Trask RS, Withers PJ, Bond IP. X-ray damage characterization in self-healing fibre reinforced polymers. *Compos Part A-Appl S* 2012;43(4):613–20.
- [15] Trask RS, Bond IP. Bioinspired engineering study of *Plantae* vasculature for self-healing composite structures. *J Roy Soc Interface* 2009;7(47):921–31.
- [16] Kousourakis A, Bannister MK, Mouritz AP. Tensile and compressive properties of polymer laminates containing internal sensor cavities. *Compos Part A-Appl S* 2008;39(9):1394–403.
- [17] Kousourakis A, Mouritz AP. The effect of self-healing hollow fibres on the mechanical properties of polymer composites. *Smart Mater Struct* 2010;19(8):085021.
- [18] Williams G, Trask R, Bond I. A self-healing carbon fibre reinforced polymer for aerospace applications. *Compos Part A-Appl S* 2007;38(6):1525–32.
- [19] Bleay S, Loader C, Hawyes V, Humberstone L, Curtis P. A smart repair system for polymer matrix composites. *Compos Part A-Appl S* 2001;32(12):1767–76.
- [20] Dong H, Esser-Kahn AP, Thakre PR, Patrick JF, Sottos NR, White SR, et al. Chemical treatment of poly(lactic acid) fibers to enhance the rate of thermal depolymerization. *ACS Appl Mater Interfaces* 2012;4(2):503–9.
- [21] Phillips DM, Ryan Pierce M, Baur JW. Mechanical and thermal analysis of microvascular networks in structural composite panels. *Compos Part A-Appl S* 2011;42(11):1609–19.

- [22] Huang C-Y, Trask RS, Bond IP. Characterization and analysis of carbon fibre-reinforced polymer composite laminates with embedded circular vasculature. *J Roy Soc Interface* 2010;7(49):1229–41.
- [23] Norris CJ, Bond IP, Trask RS. The role of embedded bioinspired vasculature on damage formation in self-healing carbon fibre reinforced composites. *Compos Part A-Appl S* 2011;42(6):639–48.
- [24] Mouritz AP, Bannister MK, Falzon PJ, Leong KH. Review of applications for advanced three-dimensional fibre textile composites. *Compos Part A-Appl S* 1999;30(12):1445–61.
- [25] Lomov SV, Bogdanovich AE, Ivanov DS, Mungalov D, Karahan M, Verpoest I. A comparative study of tensile properties of non-crimp 3D orthogonal weave and multi-layer plain weave E-glass composites. Part 1: Materials, methods and principal results. *Compos Part A-Appl S* 2009;40(8):1134–43.
- [26] Ivanov DS, Lomov SV, Bogdanovich AE, Karahan M, Verpoest I. A comparative study of tensile properties of non-crimp 3D orthogonal weave and multi-layer plain weave E-glass composites. Part 2: Comprehensive experimental results. *Compos Part A-Appl S* 2009;40(8):1144–57.
- [27] Salkind NJ, Rasmussen K. *Encyclopedia of measurement and statistics*. Thousand Oaks, Calif: SAGE Publications; 2007.
- [28] Callus PJ, Mouritz AP, Bannister MK, Leong KH. Tensile properties and failure mechanisms of 3D woven GRP composites. *Compos Part A-Appl S* 1999;30(11):1277–87.
- [29] Mouritz AP, Leong KH, Herszberg I. A review of the effect of stitching on the in-plane mechanical properties of fibre-reinforced polymer composites. *Compos Part A-Appl S* 1997;28(12):979–91.
- [30] Hamilton AR, Sottos NR, White SR. Local strain concentrations in a microvascular network. *Exp Mech* 2009;50(2):255–63.